

CHANDRA OBSERVES THE END OF AN ERA IN SN 1987A

KARI A. FRANK

Department of Astronomy and Astrophysics, Pennsylvania State University, University Park, PA 16802, USA

SVETOZAR A. ZHEKOV

Institute of Astronomy and National Astronomical Observatory, 72 Tsarigradsko Chaussee Blvd., Sofia 1784, Bulgaria

SANGWOOK PARK

Department of Physics, University of Texas at Arlington, Arlington, TX 76019, USA

RICHARD MCCRAY

Department of Astronomy, University of California, Berkeley, CA 94720-3411, USA

ELI DWEK

Observational Cosmology Laboratory, Code 665, NASA Goddard Space Flight Center, Greenbelt, MD 20771, USA

DAVID N. BURROWS

Department of Astronomy and Astrophysics, Pennsylvania State University, University Park, PA 16802, USA

ABSTRACT

Updated imaging and photometric results from *Chandra* observations of SN 1987A, covering the last 16 years, are presented. We find that the 0.5-2 keV light curve has remained constant at $\sim 8 \times 10^{-12}$ erg s⁻¹cm⁻² since 9500 days, with the 3-8 keV light curve continuing to increase until at least 10000 days. The expansion rate of the ring is found to be energy dependent, such that after day 6000 the ring expands faster in the 2-10 keV band than it does at energies < 2 keV. Images show a reversal of the east-west asymmetry between 7000 and 8000 days after the explosion. The latest images suggest the southeastern side of the equatorial ring is beginning to fade. Consistent with the latest optical and infrared results, our *Chandra* analysis indicates the blast wave is now leaving the dense equatorial ring, which marks the beginning of a major change in the evolutionary phase of the supernova remnant 1987A.

Keywords: circumstellar matter — ISM: supernova remnants — X-rays: individual (SN 1987A) — X-rays: ISM

1. INTRODUCTION

As the only nearby supernova observed in the last 400 years, SN 1987A provides the unique opportunity to study in detail the first decades of a supernova remnant's development. Over the last 28 years, SN 1987A has been evolving on timescales of months to years; reg-

ular monitoring at multiple wavelengths has therefore been crucial for tracking these changes and understanding the development of the newborn remnant. Early optical observations revealed an unusual triple ring system (Burrows et al. 1995) consisting of two outer rings and a bright equatorial ring (ER) that together form an hourglass structure. The inner ER is embedded in a larger, lower density HII region (Chevalier & Dwarkadas 1995). This circumstellar structure is likely the result of interaction between a slow, dense red supergiant wind

and the faster, lighter blue supergiant wind (Luo & McCray 1991; Wang & Mazzali 1992). The origin of this ring morphology is unclear, but may point toward either a binary-merger (Blondin & Lundqvist 1993; Morris & Podsiadlowski 2007, 2009) or fast-rotator (Chiřă et al. 2008) scenario for the progenitor star.

X-ray emission was detected by *ROSAT* 1400 days after the supernova, as the blast wave first encountered the HII region interior to the ER (Hasinger et al. 1996). Starting about 4000 days after the supernova, the blast wave began interacting with very dense ($n_e \sim 10^4 \text{ cm}^{-3}$) clumps protruding from the inner edge of the ER, visible as ‘hot spots’ in optical images (Sugerman et al. 2002) with associated X-ray emission seen with *Chandra* (Burrows et al. 2000; Park et al. 2002). Subsequent *Chandra* observations revealed impact with the main body of the ER around day 6000, resulting in a sudden decrease in the blast wave velocity (Racusin et al. 2009) and a dramatic increase in the soft X-ray flux (Park et al. 2004, 2005) as the dense material of the clumps and the ring were shock-heated. The X-ray flux has continued to rise since day 6000, indicating continuous interaction with the ER (Park et al. 2005, 2011; Maggi et al. 2012; Helder et al. 2013).

However, recent optical results suggest a transition is occurring. Fransson et al. (2015) have noted the appearance of diffuse emission and hot spots outside of the ER, beginning in 2013 (~ 9500 days). The optical hot spots, associated with the densest clumps in the ER, have also been fading since day ~ 8000 . Fransson et al. (2015) interpret this as the beginning of the clumps’ destruction by the expanding supernova ejecta. The mid-infrared emission from dust in the ER also began to fade around this time (Arendt et al. 2016).

The X-ray light curve is a straightforward and powerful probe of the circumstellar medium (CSM) density, especially given the frequent sampling with *Chandra* – approximately every 6 months with *Chandra* ACIS since day 4600. These observations have been complemented by less frequent *XMM-Newton* observations and earlier *ROSAT* fluxes. The spatially resolved *Chandra* observations also provide measurements of the ring expansion velocity and allow comparison with the morphology at optical, infrared, and radio wavelengths. Both the X-ray light curve and images have been key ingredients for constraining models of SN 1987A evolution (Chevalier & Dwarkadas 1995; Borkowski et al. 1997; Zhekov et al. 2010; Dewey et al. 2012; Orlando et al. 2015). These models predict a flattening of the light curve once the blast wave leaves the main body of the ER. The subsequent slope of the soft and hard X-ray light curves will depend on the density structure of the CSM beyond the ring (e.g. Park et al. 2011), which is unknown, as well as the properties of the ejecta, which will likely begin to

dominate the X-ray emission a few years after the blast wave leaves the ER (Orlando et al. 2015).

In this paper, we present updated *Chandra* light curves, as well as radial expansion measurements and images, covering up to 10433 days after the supernova (through 2015 September). Details of the observations and data reduction are given in §2 with the analysis and results described in §3. A discussion of these results in light of recent multiwavelength and modeling studies is provided in §4, with a summary and conclusions in §5. We assumed a distance of 51.4 kpc to SN 1987A (Panagia 1999). All uncertainties are 90% confidence unless stated otherwise.

2. OBSERVATIONS AND DATA REDUCTION

The 33 *Chandra* observations used in this work are described in Table 1. For observations through 2012, the observing configuration changed several times to reduce the effects of photon pileup, as described in Helder et al. (2013). There have been six new observations since 2012. Obs ID 16757 utilized the HRC-S/LETG, which is not affected by the molecular contamination on the ACIS optical blocking filter. The other five utilized the same ACIS/HETG configuration as previous observations, but with the observation moved back to the center of the chip to minimize the effects of contaminant absorption, which is lower and better characterized near the center of the detector. We obtained spectral and imaging results from all observations, with a few exceptions. We did not analyze the spectra of the earliest two observations, Obs IDs 1387 and 122, as the focal plane temperature was -110 C and thus there is no correction for charge transfer inefficiency. The day 7800 and 8000 epochs included observations both with and without the HETG. For these epochs we used the 0th order images and spectra from HETG observations for spectral analysis, as the use of the grating reduces pileup, and we used the bare ACIS observation for the imaging analysis, as these contain more counts. From Obs ID 16757 we did not use the HRC imaging data, only the 0.5-2 keV flux from the dispersed LETG spectrum.

Data reduction followed essentially the same procedure used in previous works (Burrows et al. 2000; Racusin et al. 2009; Park et al. 2011; Helder et al. 2013). ACIS 0th order spectra were extracted from a $4''.38$ radius circular region, with corresponding background spectra extracted from a concentric annulus with inner radius of $6''.2$ and outer radius of $12''.4$, using CIAO 4.7 and CALDB 4.6.5. While the instrument configuration was chosen to minimize pileup, Helder et al. (2013) found that modest pileup was still present in many of the observations. We followed the same procedure used in Helder et al. (2013) to correct the 0th order spectra for this pileup. The dispersed LETG spectra (positive

and negative orders) of Obs ID 16757 were extracted and binned with a minimum of 30 counts per bin.

XMM EPIC-pn fluxes through 2011 are available in Haberl et al. (2006) and Maggi et al. (2012). However, for consistency with our *Chandra* analysis and to obtain fluxes for the unpublished 2012 and 2014 *XMM* observations, we reanalyzed spectra from all EPIC-pn observations since 2001 (day 5100). Details of the observations are shown in Table 1. EPIC-pn spectra were extracted using SAS version 14, but otherwise following the procedure used by Maggi et al. (2012). It was also necessary to correct most of the EPIC-pn spectra for pileup, using the method described in the relevant SAS data analysis thread¹.

Images were obtained using the same approach as our previous works (Burrows et al. 2000; Racusin et al. 2009;

Park et al. 2011; Helder et al. 2013). Pixel randomization added by the *Chandra* software to older data sets was removed. We used split-pixel events to achieve sub-pixel resolution (Mori et al. 2001); a critical step as SN 1987A is barely resolved in raw ACIS images with a diameter of 1''.5. Images were then deconvolved with the point spread function of the telescope using the Lucy-Richardson iterative deconvolution algorithm (Lucy 1974; Richardson 1972) and smoothed by convolving with a gaussian (FWHM~0''.1). Use of the HETG changes the spectral response compared to that of the bare ACIS detector, biasing the 0th order images toward somewhat higher energies. We have two epochs which include observations both with and without the HETG. Comparing the imaging results for these observations, we found that the differences are not significant enough to change our overall results or conclusions.

Table 1. *Chandra* and *XMM* Observations, Fluxes, Radii

Obs ID	Date	Age (days)	Instrument	Exposure (ks)	0.5-2.0 keV Flux (10^{-13} erg s $^{-1}$ cm $^{-2}$)	3.0-8.0 keV Flux (10^{-13} erg s $^{-1}$ cm $^{-2}$)	Radius (arcsec)
1387	1999-10-06	4608	ACIS/HETG	68.9	0.586±0.033
122	2000-01-17	4711	ACIS	8.6	0.597±0.026
1967	2000-12-07	5036	ACIS	98.8	2.71 $^{+0.05}_{-0.05}$	0.72 $^{+0.10}_{-0.09}$	0.664±0.007
1044	2001-04-25	5175	ACIS	17.8	3.00 $^{+0.15}_{-0.15}$	0.91 $^{+0.29}_{-0.23}$	0.681±0.019
2831	2001-12-12	5406	ACIS	49.4	4.11 $^{+0.11}_{-0.11}$	0.91 $^{+0.21}_{-0.21}$	0.693±0.008
2832	2002-05-15	5560	ACIS	44.3	5.09 $^{+0.13}_{-0.13}$	1.05 $^{+0.21}_{-0.21}$	0.698±0.008
3829	2002-12-31	5789	ACIS	49.0	7.18 $^{+0.15}_{-0.14}$	1.21 $^{+0.20}_{-0.19}$	0.718±0.007
3830	2003-07-08	5978	ACIS	45.3	9.20 $^{+0.20}_{-0.20}$	1.52 $^{+0.27}_{-0.27}$	0.728±0.007
4614	2004-01-02	6157	ACIS	46.5	11.26 $^{+0.23}_{-0.23}$	1.73 $^{+0.29}_{-0.29}$	0.743±0.006
4615	2004-07-22	6359	ACIS	48.8	14.45 $^{+0.20}_{-0.21}$	1.80 $^{+0.24}_{-0.22}$	0.743±0.005
5579	2005-01-09	6530	ACIS	31.9	17.28 $^{+0.27}_{-0.26}$	1.87 $^{+0.24}_{-0.24}$	0.745±0.005
5580	2005-07-11	6713	ACIS	23.8	21.4 $^{+0.36}_{-0.35}$	2.34 $^{+0.36}_{-0.30}$	0.753±0.006
6668	2006-01-28	6913	ACIS	42.3	26.3 $^{+0.28}_{-0.28}$	2.76 $^{+0.25}_{-0.23}$	0.750±0.004
6669	2006-07-27	7094	ACIS	42.3	31.25 $^{+0.37}_{-0.35}$	3.13 $^{+0.29}_{-0.29}$	0.757±0.004
7636	2007-01-19	7270	ACIS	33.5	37.41 $^{+0.40}_{-0.38}$	3.59 $^{+0.30}_{-0.32}$	0.764±0.004
7637	2007-07-13	7445	ACIS	25.7	42.22 $^{+0.51}_{-0.50}$	3.24 $^{+0.44}_{-0.36}$	0.769±0.004
9142	2008-01-09	7624	ACIS	6.6	46.41 $^{+0.96}_{-0.96}$	3.45 $^{+0.82}_{-0.66}$	0.772±0.008
9144	2008-07-01	7799	ACIS/HETG	42.0	50.18 $^{+1.53}_{-1.52}$	4.94 $^{+0.61}_{-0.72}$...
9143	2008-07-04	7802	ACIS	8.6	0.766±0.006
10130	2009-01-05	7986	ACIS	6.0	0.786±0.008
10855	2009-01-18	8000	ACIS/HETG	18.8	55.58 $^{+2.47}_{-2.49}$	4.19 $^{+1.03}_{-0.97}$...
10222	2009-07-06	8169	ACIS/HETG	24.4	61.36 $^{+2.32}_{-2.27}$	5.17 $^{+1.04}_{-0.79}$	0.787±0.012
11090 ^a	2010-03-28	8433	ACIS/HETG	24.6	63.83 $^{+2.39}_{-2.34}$	5.61 $^{+0.77}_{-0.84}$	0.788±0.012
13131 ^a	2010-09-28	8617	ACIS/HETG	26.5	68.63 $^{+2.36}_{-2.35}$	5.75 $^{+0.76}_{-0.88}$	0.781±0.012
12539 ^a	2011-03-25	8796	ACIS/HETG	52.2	71.25 $^{+1.90}_{-1.91}$	7.29 $^{+0.61}_{-0.61}$	0.787±0.008

Table 1 continued

¹ <http://www.cosmos.esa.int/web/xmm-newton/sas-thread-epatplot>

Table 1 (*continued*)

Obs ID	Date	Age (days)	Instrument	Exposure (ks)	0.5-2.0 keV Flux (10^{-13} erg s $^{-1}$ cm $^{-2}$)	3.0-8.0 keV Flux (10^{-13} erg s $^{-1}$ cm $^{-2}$)	Radius (arcsec)
12540 ^a	2011-09-21	8975	ACIS/HETG	37.5	74.92 $^{+2.19}_{-2.16}$	7.45 $^{+0.73}_{-0.74}$	0.802 \pm 0.010
13735 ^a	2012-03-28	9165	ACIS/HETG	42.9	80.71 $^{+2.07}_{-2.20}$	8.91 $^{+0.77}_{-0.76}$	0.799 \pm 0.009
14697	2013-03-21	9523	ACIS/HETG	67.6	77.48 $^{+1.68}_{-1.66}$	9.71 $^{+0.73}_{-0.64}$	0.810 \pm 0.007
14698	2013-09-28	9713	ACIS/HETG	68.5	81.00 $^{+1.55}_{-1.55}$	11.17 $^{+0.67}_{-0.67}$	0.814 \pm 0.007
15809	2014-03-19	9885	ACIS/HETG	70.5	78.96 $^{+1.82}_{-1.73}$	11.53 $^{+0.71}_{-0.74}$	0.813 \pm 0.007
15810	2014-09-20	10071	ACIS/HETG	47.9	80.56 $^{+2.33}_{-2.32}$	11.50 $^{+0.92}_{-0.96}$	0.830 \pm 0.009
16757	2015-03-14	10246	HRC/LETG	67.6	81.21 $^{+2.68}_{-2.63}$
16756	2015-09-17	10433	ACIS/HETG	66.3	78.74 $^{+2.04}_{-2.01}$	11.97 $^{+0.75}_{-0.85}$	0.825 \pm 0.009
0083250101	2001-04-08	5158	EPIC-pn	19.2	2.91 $^{+0.10}_{-0.11}$	0.51 $^{+0.26}_{-0.25}$...
0144530101	2003-05-19	5929	EPIC-pn	67.1	8.24 $^{+0.17}_{-1.03}$	1.61 $^{+0.11}_{-0.39}$...
0406840301	2007-01-17	7268	EPIC-pn	69.2	34.76 $^{+0.14}_{-0.37}$	3.75 $^{+0.17}_{-0.12}$...
0506220101	2008-01-11	7627	EPIC-pn	75.8	44.79 $^{+0.52}_{-0.28}$	5.03 $^{+0.11}_{-0.18}$...
0556350101	2009-01-31	8013	EPIC-pn	69.6	54.71 $^{+0.47}_{-0.33}$	5.93 $^{+0.11}_{-0.18}$...
0601200101	2009-12-11	8327	EPIC-pn	76.5	62.38 $^{+0.45}_{-0.27}$	7.09 $^{+0.17}_{-0.17}$...
0650420101	2010-12-12	8693	EPIC-pn	53.1	69.87 $^{+0.54}_{-0.44}$	8.35 $^{+0.18}_{-0.27}$...
0671080101	2011-12-12	9058	EPIC-pn	61.4	75.40 $^{+0.10}_{-0.46}$	9.91 $^{+0.18}_{-0.18}$...
0690510101	2012-12-11	9423	EPIC-pn	60.1	78.68 $^{+0.17}_{-0.62}$	11.21 $^{+0.24}_{-0.23}$...
0743790101	2014-11-29	10141	EPIC-pn	57.8	78.00 $^{+0.72}_{-1.16}$	12.9 $^{+0.20}_{-0.47}$...

^a *Chandra* ACIS observations with offset chip positions.

3. ANALYSIS AND RESULTS

3.1. X-ray Light Curve

Each pileup-corrected ACIS spectrum and the LETG spectrum was fit with an absorbed two-component spectral model using XSPEC 12.8.2 (Arnaud 1996), similar to our previous works. The model consists of a cool (~ 0.3 keV) component in collisional ionizational equilibrium (`vequil`) and a warmer (~ 1.8 keV) non-equilibrium component (`vpshock`). The non-equilibrium model utilized XSPEC `nei` version 3.0, which uses the AtomDB 3.0 atomic database. The He and C abundances were fixed to those from the optical analysis of Lundqvist & Fransson (1996), Ar, Ca, and Ni to LMC values (Russell & Dopita 1992), and N, O, Ne, Mg, Si, S, and Fe to those measured by Zhekov et al. (2009) from the deep, high-resolution *Chandra* LETG and HETG observations. Absorption was fixed to 2.35×10^{21} cm $^{-2}$ (Park et al. 2006). The temperatures, normalizations, and ionization age were free parameters. The early observation Obs ID 1044, which has the lowest number of counts (1680 compared to 2420-32000 for all others observations), was fit with a single `vpshock` model that is otherwise identical to the described two-component model, as this provided a better fit. For the LETG spectra, all orders were fit simultaneously, and an additional Gaussian smoothing was included in the model. Exam-

ples of fitted ACIS spectra are shown in Figure 1. The *XMM* spectra were fit to the same model, but with a second `vpshock` component and free O, Ne, Mg, Si, S, and Fe abundances and absorbing column density. As *XMM* has much higher sensitivity than *Chandra* and therefore an order of magnitude more photons, the additional parameters were necessary to obtain fits of sufficient quality for accurate flux measurements. The best-fit absorbing column density is comparable to that used to fit the ACIS spectra, but slightly higher at $\sim 3.2 \times 10^{21}$ cm $^{-2}$. Abundances are also somewhat higher, by a factor of roughly 1.3-2, except for Fe, which is the same as our *Chandra* measurements. These differences have no significant effect on the measured fluxes, which are the primary concern here; we therefore defer further investigation to a future work. The *XMM* spectral model is comparable to that used in Maggi et al. (2012), and we obtained similar fluxes.

An important consideration in measuring the fluxes is the growing molecular contamination on the ACIS optical blocking filter (OBF) (O’Dell et al. 2013). This contamination partially absorbs the flux at energies $\lesssim 2$ keV, and is strongest at energies below 1 keV. It has evolved unpredictably, and as a result it has sometimes been difficult to obtain accurate contamination models until many months after a given observation. In the past, this

has led to inaccurately low SN 1987A flux measurements (Park et al. 2011; Helder et al. 2013). In addition, the buildup of contamination increases with distance from the chip center, and several of the SN 1987A monitoring observations used offcenter positions (to minimize pile-up by reducing the frame readout time). The contamination models are more poorly calibrated for these positions, and the measured fluxes for these observations (noted in Table 1) should be interpreted with an extra degree of caution.

We have taken several steps to mitigate contamination issues as much as possible. The most up-to-date contamination models available, version 9 released in 2014 July, have been used for the ACIS spectra. Additionally, we have obtained several independent, uncontaminated fluxes for comparison. The *Chandra* HRC detector does not suffer from contamination, so Obs ID 16757 from 2015 March utilized the HRC-S/LETG instrument configuration to obtain high-resolution spectra, from which we acquired the uncontaminated 0.5-2 keV flux. We also obtained fluxes from the *XMM* EPIC-pn observations of SN 1987A through 2014 November. Given the agreement between the ACIS, HRC-S/LETG, and *XMM* fluxes, we believe the contamination has been adequately taken into account, but it should be kept in mind that if the contamination is significantly worse than expected for the most recent observation, the associated ACIS soft flux may be slightly underestimated.

The resulting 0.5-2.0 keV and 3.0-8.0 keV fluxes are provided in Table 1 and the light curves in Figure 2. As described in previous works, there is a sharp upturn in the soft light curve around 6000 days, due to the blast wave impacting the main body of the ER (Park et al. 2005). Between 7000 and 8000 days the light curve changes again, such that the flux increases linearly rather than exponentially (Helder et al. 2013). The latter change indicates the average density of new material encountered by the blast wave stopped increasing around that time. The soft band flux (0.5-2 keV) since day 9500 has remained approximately constant; such a leveling off of the light curve is expected to happen when the blast wave leaves the dense ring (e.g. Park et al. 2011). In contrast, the hard light curve has overall exhibited slower growth with fewer changes over time, increasing steadily until at least day ~ 10000 .

The changes in the light curves are also reflected in the ratio of the 3.0-8.0 keV to 0.5-2.0 keV band fluxes and the normalizations of the cool and warm components of the spectral model, shown in Figures 3 and 4. The model normalization parameters represent the scaled volume emission measures. The X-ray emission continuously softens until about day 7500, when both the band ratio and the cool component normalization

abruptly flatten. The band ratio then begins to slowly increase, with a possible flattening in the last 2 or 3 observations.

3.2. Imaging

Images from all our *Chandra* epochs are shown in Figure 5. Initially brightest in the east, the ER becomes obviously brighter in the west by 8433 days and has remained that way through the most recent observation. A plot of the fraction of the total flux in the east and west halves over time demonstrates that reversal of the asymmetry occurred between 7000 and 8000 days (Figure 6). The most recent image at 10433 days suggests the southeastern quadrant of the ER is beginning to fade out, while the west remains bright.

3.3. Expansion

The superb spatial resolution of *Chandra* enables us to measure the radial expansion of the ER. This was done following the method of Racusin et al. (2009), wherein each deconvolved image was fit to a spatial model that consists of four lobes and a ring. The best fit radii are shown in Figure 7. We carried out this procedure for images in the 0.3-8 keV, 0.3-0.8 keV, 0.5-2 keV, and 2-10 keV bands. The resulting best fit radii for the 0.3-8 keV band are given in Table 1. A simple broken-linear function was fit to the results for each band to estimate expansion velocities. The statistics are worse for the 0.3-0.8 keV and 2-10 keV bands due to the lower number of counts in these bands for many of the observations, especially after insertion of the HETG. This is reflected in the substantially larger error bars. For each band, observations which had insufficient counts (\lesssim few hundred) for robust image fitting were excluded from the expansion analysis.

The time of impact with the main ER and the velocities before and after this event were determined from the fit to the 0.3-8 keV images. Impact with the ER occurred at 6047 ± 110 days. The velocities (i.e. the slopes of the expansion curve) are 6711 ± 787 km s $^{-1}$ before this date and 1854 ± 101 km s $^{-1}$ afterward. The early velocity decreases slightly to 6104 ± 849 km s $^{-1}$ if the earliest two observations, with large error bars, are excluded. These results are consistent with the earlier estimates of Racusin et al. (2009) and Helder et al. (2013) using the same method.

It is also informative to compare the expansion of the ER in multiple bands. The standard ‘soft’ band of 0.5-2 keV contains most of the counts, and therefore appears essentially the same as the 0.3-8 keV expansion. The softest emission, 0.3-0.8 keV, which corresponds to emission from the densest regions, is similar to the broad band, both in the ring size and expansion velocity, until impact with the ER at ~ 6000 days. After this date,

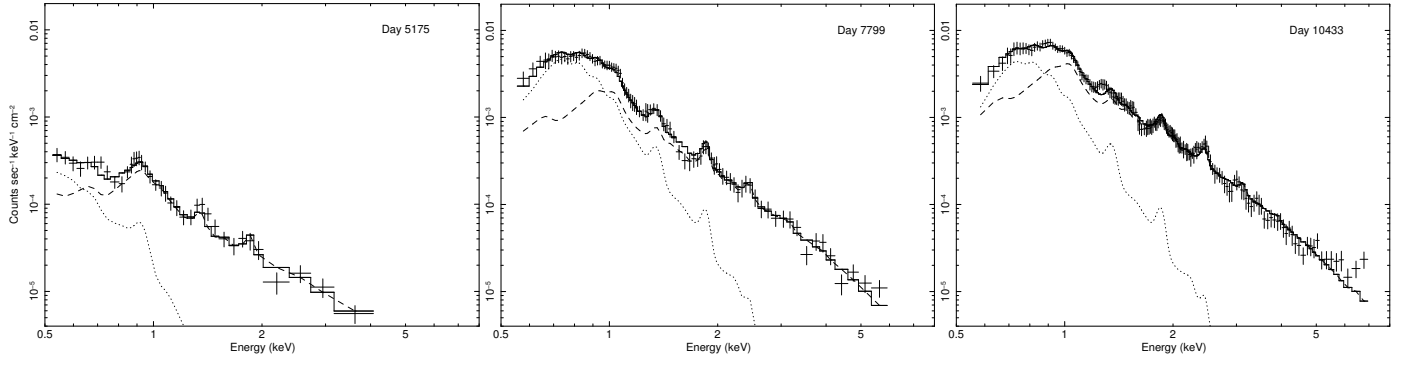


Figure 1. ACIS spectra and their best-fit models from days 5175 (left), 7799 (center), and 10433 (right). The cool (~ 0.3 keV) and warm (~ 1.8 keV) components are also shown as dotted and dashed lines respectively.

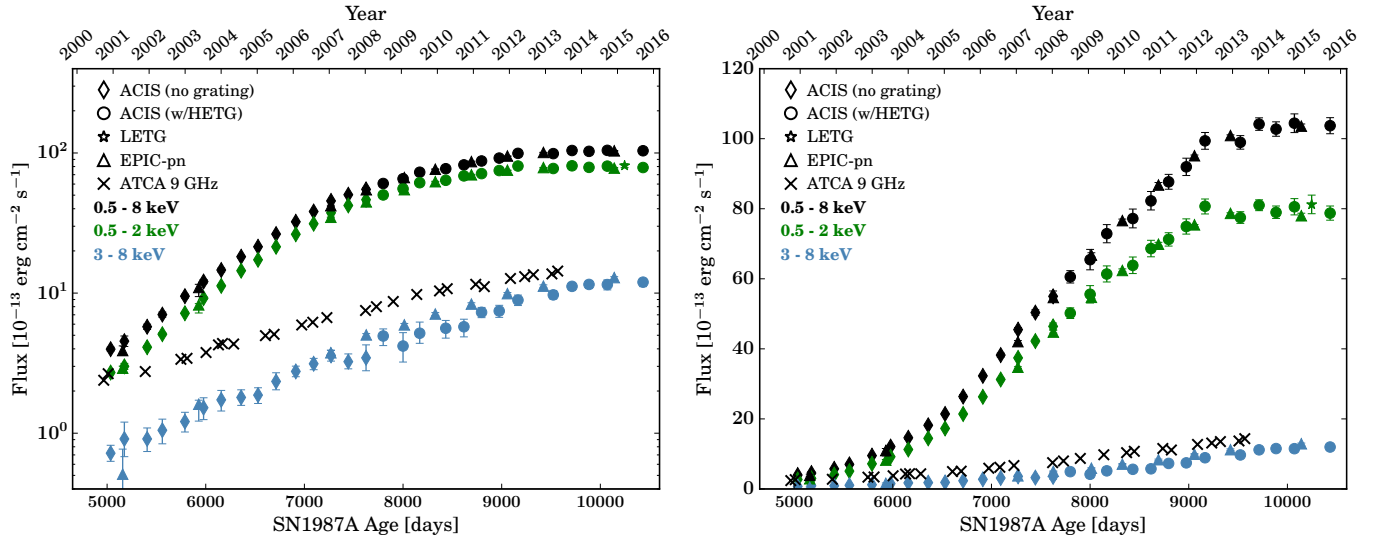


Figure 2. X-ray light curve of SN 1987A from days 5036 through 10433, shown with fluxes on both a log (left) and linear (right) scale. *Chandra* ACIS fluxes are given as diamonds (bare ACIS observations) and circles (ACIS observations with HETG), and the stars are LETG fluxes from the 2015 March observation. *XMM-Newton* EPIC-pn fluxes are shown as triangles. The 0.5-8.0 keV fluxes are in black, 0.5-2.0 keV in green, and 3.0-8.0 keV in blue. The 9 GHz ATCA fluxes from [Ng et al. \(2013\)](#), arbitrarily scaled, are shown as crosses. Note that for many points the error bars are too small to be visible.

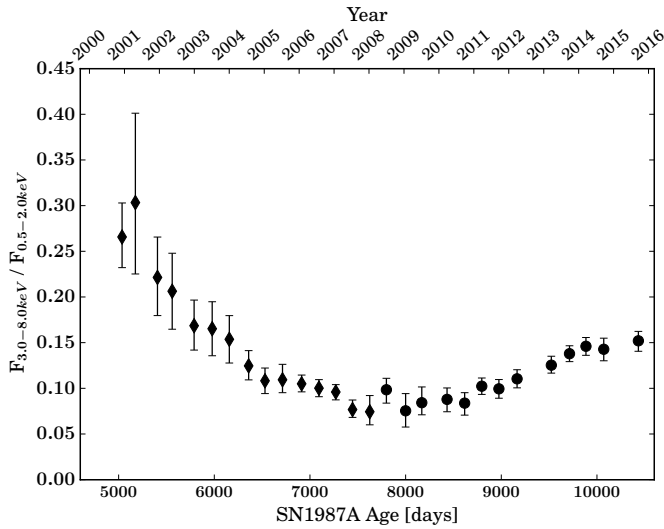


Figure 3. Ratio of the 3-8 keV to 0.5-2 keV ACIS fluxes from days 5036 to 10433. The symbols are the same as in Figure 2.

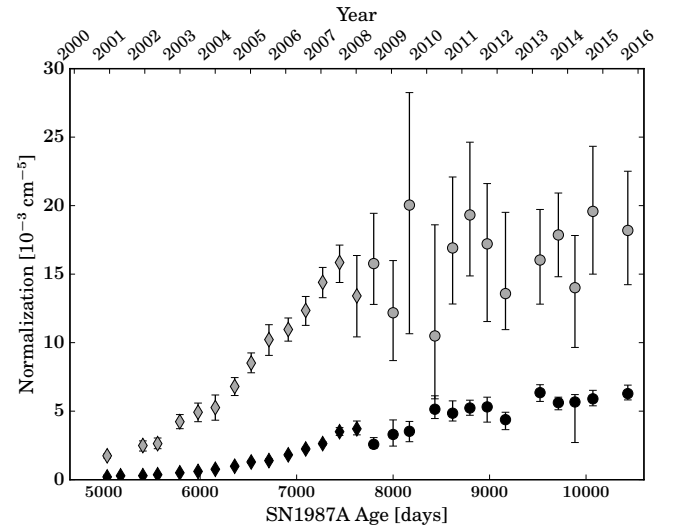


Figure 4. Normalizations of the cool (gray) and warm (black) spectral model components from days 5036 to 10433. The symbols are the same as in Figure 2.

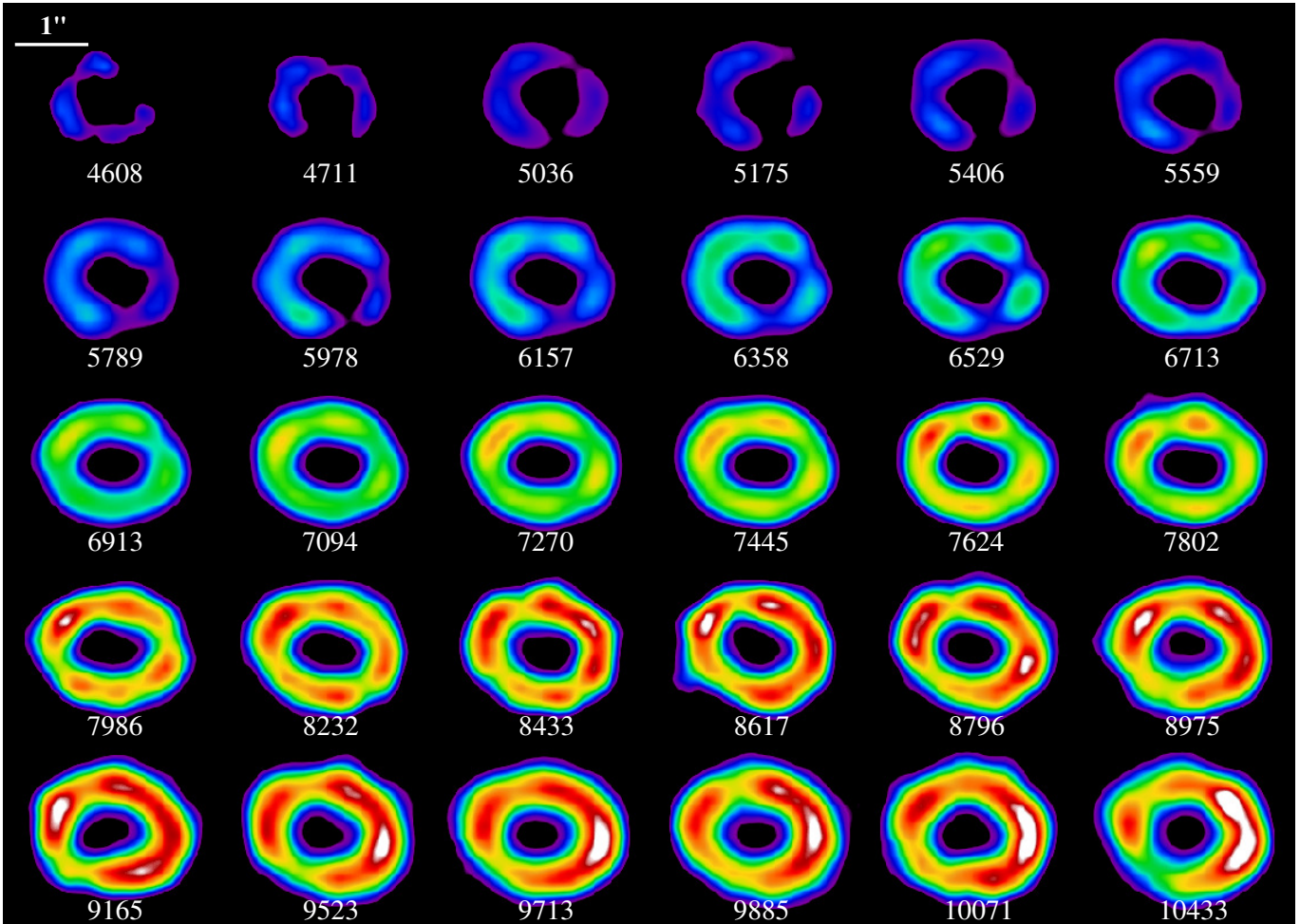


Figure 5. Deconvolved, smoothed 0.3-8.0 keV false-color images of SN 1987A covering days 4608 - 10433. Images use a square root scale and are normalized by flux. The age, in days since the supernova, is shown below each image. North is up and East is to the left.

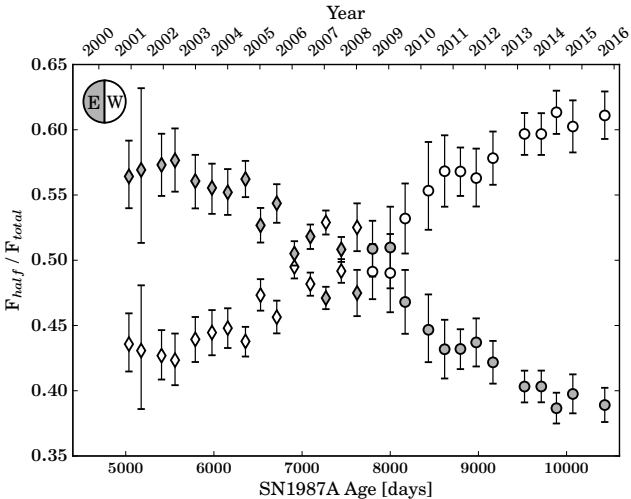


Figure 6. Fraction of the total 0.3-8 keV flux in the east (filled symbols) and west (empty symbols) halves of the ER over time. The center of the ring for each observation is defined as the center of the ring from our best-fit model as described in §3.3. Symbols are the same as Figure 2. The fractional fluxes of the individual southeast and northeast quadrants evolve similarly over time (both decreasing), as do the western quadrants (both increasing).

expansion in this band becomes consistent with zero. The hard band (2-10 keV) appears to have a slightly later break point, at 6530 ± 352 days. Prior to this it has a similar velocity to the other bands but smaller radii. After ER impact, the velocity is faster than the softer bands, 3071 ± 299 km s⁻¹, and similar to the radio expansion velocities, ~ 3900 km s⁻¹ (Ng et al. 2013; Zanardo et al. 2013). Between 8000 and 9000 days the radii in the hard band overtake those of the 0.3-0.8 keV band and catch up to the 0.5-2 keV band. Currently, the size of the ER in the hard band is similar to that in the 0.3-8 keV and 0.5-2 keV bands, while the 0.3-0.8 keV radius is significantly smaller. These energy-dependent expansion rates are a likely a result of the shock velocity being slower through denser material.

4. DISCUSSION

The ER can be modeled as a smooth ring with $n \sim 10^3$ cm⁻³ and very dense clumps, $n \sim 10^4$ cm⁻³, distributed around the inner edge of the smooth ring (Dewey et al. 2012; Orlando et al. 2015). The X-ray emission arises from a complex system of transmitted

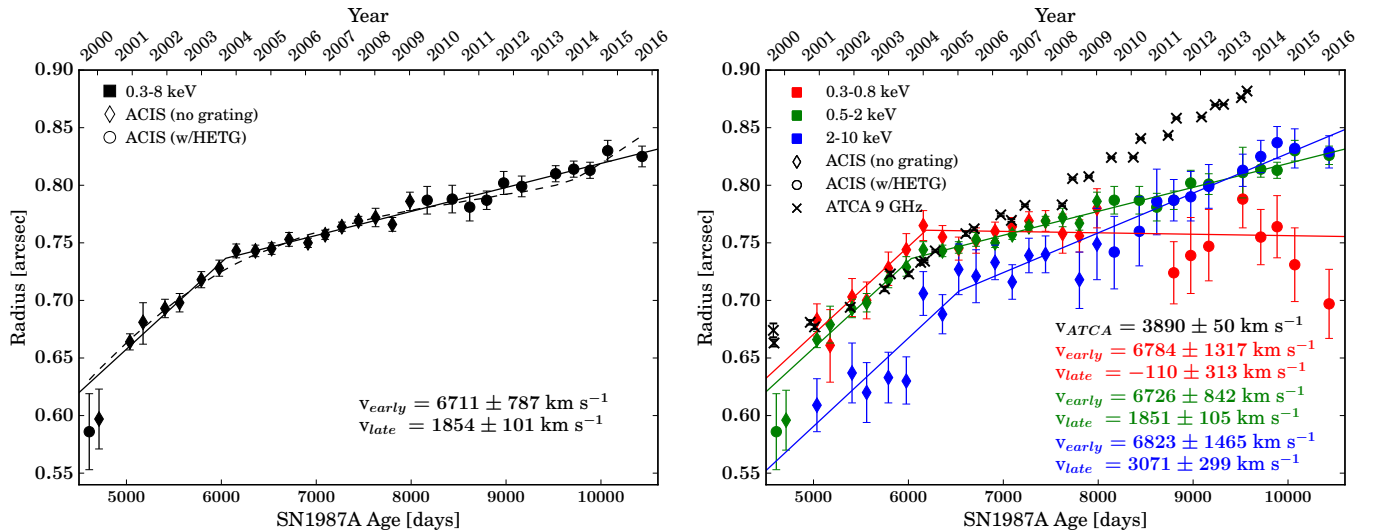


Figure 7. Best-fit radii of the ER from the ring plus 4-lobe model fits. On the left is the result from fitting to the broad band (0.3–8 keV) images. On the right are the results to fitting to the 0.3–0.8 keV (red), 0.5–2 keV (green), and 2–10 keV (blue) images. The crosses show the semi-major axis of the ER at 9 GHz from [Ng et al. \(2013\)](#). A simple broken-linear fit to each band is also shown as a solid line of the corresponding color, with the resulting velocities with 1σ errors noted for the early and late epochs (before and after ~ 6000 days, respectively). [Ng et al. \(2013\)](#) found the radio expansion was better fit with a simple linear model; the velocity from their linear fit is also given. In the left panel, an analytical density profile was used to fit the 0.3–8 keV expansion, as discussed in §4, and the resulting fit is shown as a dashed line.

and reflected shocks as the blast wave interacts with these various CSM components ([Zhekov et al. 2009, 2010](#); [Dewey et al. 2012](#)). While the actual physical picture is quite complicated, for the purposes of interpreting the X-ray observations the emission can be characterized by a ‘cool’ (~ 0.3 keV), or soft, component and a ‘warm’ (~ 1.5 –3 keV), or hard, component. The cool component represents the slow transmitted shocks in the dense clump material and is responsible for the majority of the soft X-ray emission after ~ 6000 days ([Zhekov et al. 2010](#); [Dewey et al. 2012](#); [Orlando et al. 2015](#)). The warm component is representative of the shocks moving through the lower density ring material, including reflected shocks, and contributes most of the hard emission ([Zhekov et al. 2010](#); [Orlando et al. 2015](#)).

Between days 6000 and 7000 the steep increase of the soft X-ray light curve is due to the blast wave interacting with the dense clumps. The resulting transmitted shocks in the clumps moved more slowly than the shocks moving through the inner HII region or the smooth component of the ER. This can be seen in the X-ray expansion, shown in Figure 7, of the 0.3–0.8 keV band. This emission is dominated by the densest clump emission which slowed the transmitted shock dramatically, such that the measured expansion velocity is consistent with zero after day 6000. Expansion in the 0.5–2 keV band, which contains most of the X-ray counts and includes contributions from both the clumps and smooth component of the ring, also slowed significantly after day 6000, to a velocity of 1854 km s^{-1} . This velocity is consistent with that derived by [Dewey et al. \(2012\)](#) from hydrodynamical modeling of the high-resolution X-ray spectra.

We can also estimate the density jump required to cause the observed deceleration as the blast wave moved from the HII region into the ER. [Zhekov et al. \(2010\)](#) assumed an analytical density profile that provides an analytical solution to the expansion curve (see §3.1 of [Zhekov et al. 2010](#)). We fit this model to the 0.3–8 keV expansion curve; the result is shown in Figure 7 (left). Our best-fit model requires that the density increases by a factor of 10.6 ± 1.6 . Given that the HII region has densities of $\sim 10^2 \text{ cm}^{-3}$, this indicates that the expansion is primarily related to the smooth ring component, with a typical density on the order of 10^3 cm^{-3} . For this epoch, from days 6500 – 8000, [Dwek et al. \(2010\)](#) found the infrared-to-X-ray band flux ratio was approximately constant, implying X-ray heating of dust in the ER. Throughout this period, the optical flux continuously increased ([Fransson et al. 2015](#)) as transmitted shocks moved through the clumps.

The hard X-ray light curve is dominated by emission from the smooth component and so increases more slowly, resulting in the sharp decline of the band ratio (Figure 3) before day 7500. This behavior is also evident in our 2-component spectral fits, shown in Figure 1. Until ~ 7500 days the cool component increased much more rapidly than the warm component (Figure 4). The radio light curve and expansion resemble those of the hard X-rays (Figures 2 and 7). The similar evolution of the hard X-rays and the radio suggests the radio emission also originates from the smooth ring component.

After ~ 7500 days, both the optical and mid-infrared emission from the ER began to fade ([Fransson et al. 2015](#); [Arendt et al. 2016](#)), which is interpreted as the re-

sult of destruction of the clumps and dust, respectively. Around this time, we find the growth of the soft X-ray light curve transitions from exponential to linear (Figure 2) and the band ratio flattens (Figure 3), which suggest there is little emission from newly shocked clump material. We can use this to place some rough limits on the lengths of the clumps, which likely have a range of different sizes, radial distances, and shock velocities. The largest possible clump (i.e. the longest protrusion) would have been encountered by the forward shock between 4000 and 5000 days (coincident with the appearance of the first hot spots), with the resulting transmitted shock traversing the entire clump by day 8000 (the approximate end of shock-clump interaction). For a velocity of 1854 km s^{-1} , as found in our expansion measurements, this implies a length of $\sim 6.4 \times 10^{16} \text{ cm}$. The smallest clumps would have been encountered by day 6045 (onset of full interaction with the ER) with the shocks exiting around day 7000 (the first signs of decreasing shock-clump interaction), implying a length of $\sim 1.5 \times 10^{16} \text{ cm}$. This is comparable to the $1.7 \times 10^{16} \text{ cm}$ clump size estimated by Orlando et al. (2015) with their simple clump model.

During the post-clump phase, shocks were still moving through the smooth ring component and thus both the hard X-ray light curve and expansion continue to increase as before. Comparing the ACIS spectra at days 7799 and 10433 (Figure 1), it is clear that the cool component did not increase, while the warm component has continued to grow. This explains the observed flattening of the band ratio at ~ 7500 days (Figure 3) and the slow increase afterwards as soft emission from the clumps very slowly begins to fade while the soft and hard emission from the smooth component both continue to increase at a steady rate. There is no detectable change in the expansion velocity, as expected if the observed expansion is mainly that of the shock moving through the smooth ring.

The soft X-ray light curve leveled off at $\sim 8 \times 10^{-12} \text{ ergs s}^{-1} \text{ cm}^{-2}$ by day 9500. Such a flattening of the light curve has been predicted to occur when the forward shock finally leaves the ER (Park et al. 2011; Dewey et al. 2012; Orlando et al. 2015). In this same period new optical emission was seen by Fransson et al. (2015) outside of the ER, as both faint hot spots and diffuse emission. This is interpreted as gas that is either directly shocked by the blast wave or heated by X-rays from the outer edge of the ER. In either case, this lends support to the idea that the forward shock is now beginning to propagate into the region beyond the ER.

While the X-ray emission has thus far been dominated by the shocked HII material (prior to day 4000) and then the shocked ER material, the simulations of Orlando et al. (2015) determined that the flux from the

reverse-shocked ejecta was also steadily growing. As the reverse shock continues to encounter more ejecta and the emission from the ER begins to fade, emission from the ejecta will become the dominant source of X-rays. Orlando et al. (2015) predict this transition will occur within the next five years.

The evolution of X-ray morphology, dominated by soft emission, is similar to the optical. The optical hot spots and the X-ray emission first appeared on the eastern side of the ER (Sugerman et al. 2002; Fransson et al. 2015), and the radio emission is also stronger in the east (Ng et al. 2013; Zanardo et al. 2014). Fransson et al. (2015) found that the hot spots on the eastern side began to fade around day 7000, while those in the west did not begin to fade until ~ 1500 days later. The asymmetry in the X-ray emission reversed during this time, becoming brighter in the west by about 8000 days, as seen in Figures 5 and 6. By day 10433, X-ray emission in the east has clearly started to weaken, especially in the southeast quadrant where the optical emission has also faded the most.

As with the light curve and expansion, the radio morphology matches that of the hard X-rays better than the soft (Figure 8). They evolve similarly to the optical and the overall X-ray, but are delayed by roughly 2000 days. In the 2-10 keV band, the east-west asymmetry began to reverse only around day 9500 (Figure 9), compared to ~ 7500 days for the 0.3-8 keV emission. Ng et al. (2013) found similar behavior for the 9 GHz images, which remained brightest in the east until at least 9568 days. Zanardo et al. (2013) also measured larger radio expansion velocities in the east than the west.

This behavior suggests the evolution of the remnant has been delayed in the west compared to the east, implying either an asymmetric expansion of the blast wave, asymmetries in the CSM density profile, or both. The first case implies an asymmetric explosion, while the second case implies asymmetries in the progenitor winds. Interestingly, Zanardo et al. (2014) found residual emission offset slightly west of the ER center in ATCA and ALMA observations which is suggestive of a pulsar wind nebula (PWN); if this tentative PWN emission is confirmed, it would imply the central pulsar received a westward kick along with a corresponding higher energy outflow to the east.

We do not yet detect any emission from a central object. To obtain a simple estimate of the upper limit on the flux, we added a central point source to the best-fit model image and increased the flux until the χ^2 value increased by 2.706, corresponding to the 90% confidence limit. For the 2015 September observation (Obs ID 16756), we find a limit of $9 \times 10^{-4} \text{ counts s}^{-1}$ in the 2-10 keV band. Stacking observations resulted in a maximum 2-10 keV count rate of $6 \times 10^{-4} \text{ counts}$

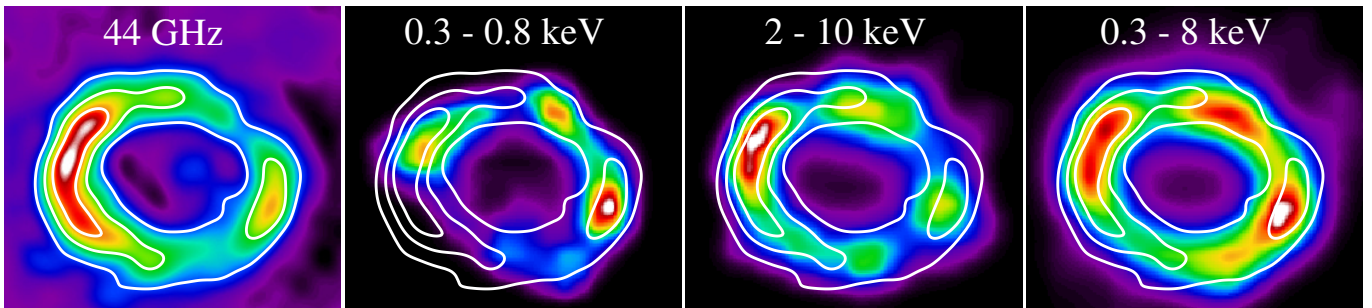


Figure 8. From left to right, the 44 GHz (from Zanardo et al. 2013), 0.3-0.8 keV, 2-10 keV, and 0.3-8 keV images, with the 44 GHz contours overlaid in white. All images are from 2011 March (~ 8800 days). There is good agreement between the broad band X-ray and the radio emission, while the hard X-rays match the radio better than the very soft 0.3-0.8 keV band.

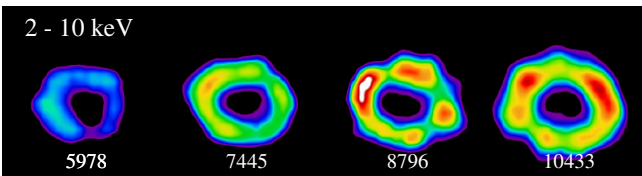


Figure 9. 2-10 keV images at roughly 4 year intervals, with the age in days shown underneath. Prior to ~ 9500 days, the 2-10 keV images always peak in the east (to the left), with a slow decrease in this asymmetry over time. Since 9500 days, it has been more symmetric and may now be slightly brighter in the west. Compare this to the broad band images (dominated by softer emission), which are clearly brightest in the west by day 8433. (Figures 5 and 6).

s^{-1} . Assuming a nonthermal spectrum with a typical power law of index $\Gamma = 1.5$ and $N_H = 0.235 \times 10^{22} \text{ cm}^{-2}$, these translate to $L_{X,16756} \lesssim 1.5 \times 10^{34} \text{ erg s}^{-1}$ and $L_{X,stacked} \lesssim 3.1 \times 10^{33} \text{ erg s}^{-1}$, respectively. Orlando et al. (2015) estimate the local absorbing column density in the center of the ER to be $\sim 5 \times 10^{22} \text{ cm}^{-2}$, 20 times higher than interstellar absorption along the line of sight and far too high to allow detection of faint emission from a central point source. Assuming this higher absorption, we obtain limits on the intrinsic luminosity of $L_{X,16756} \lesssim 3.3 \times 10^{34} \text{ erg s}^{-1}$ and $L_{X,stacked} \lesssim 1.2 \times 10^{34} \text{ erg s}^{-1}$. In general, the strong X-ray emission from the ER hampers detection of a faint central source; the putative central object can probably not be detected in the X-ray band unless the emission from the ring and other sources (such as shocked ejecta) fades, the internal absorption decreases, or both.

5. CONCLUSIONS

We report our imaging and photometric results from 31 epochs of *Chandra* observations of SN 1987A, covering 16 years. Our results are consistent with the overall physical picture of a smooth ER ring with dense clumps embedded around the inner edge. Changes in the soft X-ray light curve and reversal of the east-west asymmetry between 7000 and 8000 days are consistent with the optical and infrared results which demonstrate the end of shock interaction with the dense clumps at this time. After day 8000 shocks continue to move through

the smooth ring component, which has a lower density than the clumps, resulting in increasing X-ray flux until ~ 9500 days. The 0.5-2 keV light curve then levels off at $\sim 8 \times 10^{-12} \text{ ergs s}^{-1} \text{ cm}^{-2}$, while the latest image indicates the eastern side of the ER is beginning to fade, evidence that the blast wave has moved into a lower density region beyond the ER. Evolution of the morphology implies an asymmetric evolution of the newborn remnant, with the above development delayed in the west compared to the east. This asymmetry is evidence of asymmetry in the explosion, the CSM density profile, or both. Similarities in the hard X-ray and radio light curves, expansion, and morphologies suggest both the hard X-ray and radio emission originate from the same region, likely the smooth component of the ring.

Future observations of the X-ray light curve and morphology will trace the density profile of the material outside the ER, which is currently unknown and records the history of the progenitor's stellar wind. These observations can aid in distinguishing between different models of the progenitor's evolution. Additionally, the impending brightening of the ejecta will soon allow measurements of its composition and structure via *Chandra* observations, placing constraints on properties of the supernova and the progenitor star. Emission from the reverse-shocked ejecta may also help reveal the origin of the observed east-west asymmetry.

The authors would like to thank G. Zanardo for providing the 44 GHz images and P. Broos for assistance with the ACIS pileup correction. The scientific results reported in this article are based on observations made by the Chandra X-ray Observatory and have made use of software provided by the Chandra X-ray Center in the application package CIAO. Support for this work was provided by the National Aeronautics and Space Administration through Chandra Award Numbers GO3-14058X, GO4-15056X, and GO5-16054X issued by the Chandra X-ray Observatory Center, which is operated by the Smithsonian Astrophysical Observatory for and on behalf of the National Aeronautics Space Adminis-

tration under contract NAS8-03060.

REFERENCES

- Arendt, R. G., Dwek, E., Bouchet, P., et al. 2016, *AJ*, 151, 62
- Arnaud, K. A. 1996, in *ASP Conference Series*, Vol. 101, *Astronomical Data Analysis Software and Systems V*, ed. G. H. Jacoby & J. Barnes, 17
- Blondin, J. M., & Lundqvist, P. 1993, *ApJ*, 405, 337
- Borkowski, K. J., Blondin, J. M., & McCray, R. 1997, *ApJ*, 477, 281
- Burrows, C. J., Krist, J., Hester, J. J., et al. 1995, *ApJ*, 452, 680
- Burrows, D. N., Michael, E., Hwang, U., et al. 2000, *ApJ*, 543, L149
- Chevalier, R. A., & Dwarkadas, V. V. 1995, *ApJ*, 452, L45
- Chiță, S. M., Langer, N., van Marle, A. J., García-Segura, G., & Heger, A. 2008, *A&A*, 488, L37
- Dewey, D., Dwarkadas, V. V., Haberl, F., Sturm, R., & Canizares, C. R. 2012, *ApJ*, 752, 103
- Dwek, E., Arendt, R. G., Bouchet, P., et al. 2010, *ApJ*, 722, 425
- Fransson, C., Larsson, J., Migotto, K., et al. 2015, *ApJ*, 806, L19
- Haberl, F., Geppert, U., Aschenbach, B., & Hasinger, G. 2006, *A&A*, 460, 811
- Hasinger, G., Aschenbach, B., & Truemper, J. 1996, *A&A*, 312, L9
- Helder, E. A., Broos, P. S., Dewey, D., et al. 2013, *ApJ*, 764, 11
- Lucy, L. B. 1974, *AJ*, 79, 745
- Lundqvist, P., & Fransson, C. 1996, *ApJ*, 464, 924
- Luo, D., & McCray, R. 1991, *ApJ*, 379, 659
- Maggi, P., Haberl, F., Sturm, R., & Dewey, D. 2012, *A&A*, 548, L3
- Mori, K., Tsunemi, H., Miyata, E., et al. 2001, in *ASP Conference Series*, Vol. 251, *New Century of X-ray Astronomy*, ed. H. Inoue & H. Kunieda, 576
- Morris, T., & Podsiadlowski, P. 2007, *Sci*, 315, 1103
- . 2009, *MNRAS*, 399, 515
- Ng, C.-Y., Zanardo, G., Potter, T. M., et al. 2013, *ApJ*, 777, 131
- O'Dell, S. L., Swartz, D. A., Tice, N. W., et al. 2013, in *SPIE Conf. Ser.*, Vol. 8859, *UV, X-Ray, and Gamma-Ray Space Instrumentation for Astronomy XVIII*, ed. O. H. Siegmund, 88590F
- Orlando, S., Miceli, M., Pumo, M. L., & Bocchino, F. 2015, *ApJ*, 810, 168
- Panagia, N. 1999, in *IAU Symposium*, Vol. 190, *New Views of the Magellanic Clouds*, ed. Y. Chu, N. Suntzeff, J. Hesser, & D. Bohlender, 549
- Park, S., Burrows, D. N., Garmire, G. P., et al. 2002, *ApJ*, 567, 314
- Park, S., Zhekov, S. A., Burrows, D. N., Garmire, G. P., & McCray, R. 2004, *ApJ*, 610, 275
- Park, S., Zhekov, S. A., Burrows, D. N., et al. 2006, *ApJ*, 646, 21
- Park, S., Zhekov, S. A., Burrows, D. N., & McCray, R. 2005, *ApJ*, 634, L73
- Park, S., Zhekov, S. A., Burrows, D. N., et al. 2011, *ApJ*, 733, L35
- Racusin, J. L., Park, S., Zhekov, S. A., et al. 2009, *ApJ*, 703, 1752
- Richardson, W. H. 1972, *JOSA*, 62, 55
- Russell, S. C., & Dopita, M. A. 1992, *ApJ*, 384, 508
- Sugerman, B. E. K., Lawrence, S. S., Crotts, A. P. S., Bouchet, P., & Heathcote, S. R. 2002, *ApJ*, 572, 209
- Wang, L., & Mazzali, P. A. 1992, *Natur*, 355, 58
- Zanardo, G., Staveley-Smith, L., Ng, C.-Y., et al. 2013, *ApJ*, 767, 98
- Zanardo, G., Staveley-Smith, L., Indebetouw, R., et al. 2014, *ApJ*, 796, 82
- Zhekov, S. A., McCray, R., Dewey, D., et al. 2009, *ApJ*, 692, 1190
- Zhekov, S. A., Park, S., McCray, R., Racusin, J. L., & Burrows, D. N. 2010, *MNRAS*, 407, 1157